Available online at www.sciencedirect.com
ScienceDirect
Earth and Planetary Science Letters 252 (2006) 189–200
EPSL
www.elsevier.com/locate/epsl

Teleseismic tomography reveals no signature of the Dead Sea Transform in the upper mantle structure

Ivan Koulakov [a,b], Stephan V. Sobolev [a,d,*], Michael Weber [a,c], Sergey Oreshin [d], Kurt Wylegalla [a], Rami Hofstetter [e]

[a] GeoForschungsZentrum-Potsdam, Germany
[b] Institute of Geology SB RAS, Novosibirsk, Russia
[c] University of Potsdam, Potsdam, Germany
[d] Institute of Physics of the Earth, RAS, Moscow, Russia
[e] Geophysical Institute of Israel, Lod, Israel

Received 3 November 2005; received in revised form 25 September 2006; accepted 26 September 2006
Available online 2 November 2006
Editor: R.D. van der Hilst

Abstract

We present results of a tomographic inversion of teleseismic data recorded at 48 stations of a temporary network which was installed in the area of the Dead Sea Transform (DST) and operated for 1 yr in the framework of the multidisciplinary DESERT Project. The 3366 teleseismic P and PKP phases from 135 events were hand picked and corrected for surface topography and crustal thickness. The inversion shows pronounced low-velocity anomalies in the crust, beneath the DST, which are consistent with recent results from local-source tomography. These anomalies are likely related to the young sediments and fractured rocks in the fault zone. The deeper the retrieved anomalies are quite weak. Most prominent is the high-velocity strip-like anomaly striking SE–NW. We attribute this anomaly to the inherited heterogeneity of lithospheric structure, with a possible contribution by the shallow Precambrian basement east of the DST and to lower crustal heterogeneity reported in this region by other seismic studies. We do not observe reliable signature of the DST in the upper mantle structure. Some weak indications of low-velocity anomalies in the upper mantle beneath the DST may well result from the down-smearing of the strong upper crustal anomalies. We also see very little topography of the lithosphere–asthenosphere boundary beneath the DST, which would generate significant horizontal velocity variations. These results are consistent with predictions from a recent thermo-mechanical model of the DST. Our tomographic model provides some indication of hot mantle flow from the deeper upper mantle rooted in the region of the Red Sea. However, resolution tests show that this anomaly may well be beyond resolution of the model.

Keywords: teleseismic tomography; Dead Sea Transform; lithosphere; asthenosphere; tectonophysics

1. Introduction

The region of interest (Fig. 1) covers the Dead Sea Transform (DST) area between the Gulf of Aqaba in the south, and the Dead Sea basin in the north (length of about 250 km), and from the Eastern Mediterranean

* Corresponding author. GeoForschungsZentrum-Potsdam, Germany.
E-mail address: stephan@gfz-potsdam.de (S.V. Sobolev).

0012-821X/$ - see front matter © 2006 Elsevier B.V. All rights reserved.
doi:10.1016/j.epsl.2006.09.039

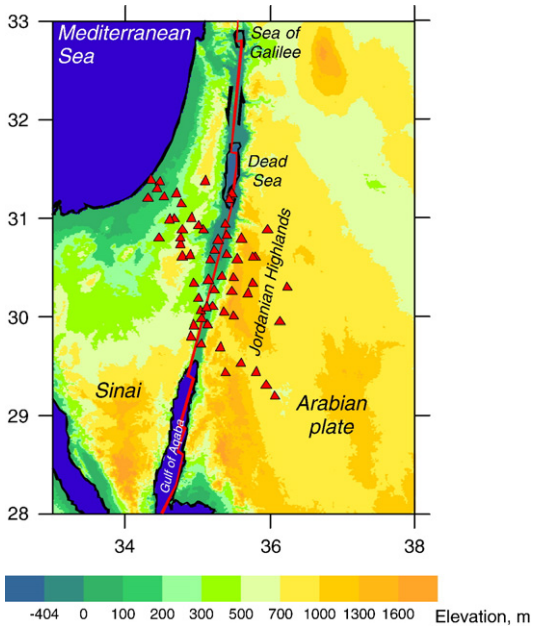

Fig. 1. Relief of the study area and distribution of the seismic stations used (red triangles). Red line shows approximately the position of the Dead Sea Transform (DST).

coast in the north-west, to the Jordanian highlands in the east (width of about 200 km). The DST fault (red line in Fig. 1) separates the Arabian plate from the African plate and links the divergent plate boundary in the Red Sea with the convergent plate boundary in southern Turkey. The tectonic activity in the study area is mostly determined by the activity of this transform which has taken about 105 km of left-lateral strike–slip displacement during the last 15–20 Myr. The key questions concerning the deep structure of this region are whether the DST itself leaves a seismic signature in the underlying mantle or does it separate mantle domains with significantly different physical properties. The way to address these questions is through teleseismic tomography.

Teleseismic tomography is a powerful tool used to derive information about deep anomalies in the Earth, using travel times recorded by a regional network from distant sources (usually at distances of more than 20°). This method has been developed since the seventies [1] and has been successfully used for the investigation of different regions (e.g. [2–5]). The images of seismic anomalies are then used for the estimation of the distribution of temperature, density and other parameters [6], which then can be used for geodynamic numerical modeling, gravity inversion [2,7] and other applications.

In this study we invert teleseismic data recorded by a temporary seismic network which was installed in the area of the Dead Sea Transform (DST) in the framework of the DESERT Project [8,9]. Several factors ensure a high quality of the data: clear phases, high accuracy of picks, large number of stations which recorded each individual event, as well as the fact that the phases from all the stations were processed simultaneously by a single highly experienced person. First we apply the usual inversion technique and obtain an image of the deep structure of the area down to 280 km depth. After examination of the resolution of the model using different tests we develop a simplified synthetic model which, after processing through the inversion procedure, generates the same major features (in respect to shape and amplitude), provides the same travel time residuals and has the same variance reduction as the tomographic model. We then discuss this model together with other seismic data in the DST region and the tomographic image of another continental transform fault (Altyn Tagh fault in northern Tibet) and compare our results with expectations from a recent thermo-mechanical model of the DST [11].

2. Previous studies

Before the DESERT project, several geophysical studies have been performed to investigate the crustal structure in the area of the DST, such as refraction–reflection profiles [e.g. 12–14], gravity [15,16], receiver function [17,18], complex seismic, gravity and magnetic studies [19] and local tomography based on the ISC data [20]. The multidisciplinary DESERT project [8] covers several geophysical disciplines: seismic profiling [9,21], seismology [22–24], magnetotellurics [25], gravity and numerical modeling [11]. The observations suggest that the crustal thickness in this region increases gradually from West to East without visible sharp steps. Under the coast of the Mediterranean the crustal thickness is estimated to be about 25 km, while under the Jordanian highlands it reaches 38 km.

The upper mantle structure beneath this region has been studied using teleseismic tomography [26] based on data recorded by the Israeli Seismic Network and several Jordanian stations located on the eastern side of the DST. Information about the main seismic boundaries (Moho, 420 km and 670 km) under the same region has been obtained on the basis of receiver function analysis [18,24]. These studies reveal no significant variations of seismic parameters across the DST. However, teleseismic tomography [26] shows a weak decrease of P-velocity in the uppermost mantle under the eastern flank of the transform.

Recently, Sobolev et al. [11] performed thermo-mechanical modeling of the DST, where they studied the

mechanism of shear strain localization in a heterogeneous rheologically stratified lithosphere and also attempted to reproduce the geological evolution and lithospheric structure of the DST in the Arava/Araba Valley. One prediction of this modeling study is the thermal structure of the mantle, which can be converted into seismic structure using mineral physics constraints [6].

The study presented here is a continuation of the teleseismic study by Hofstetter et al. [26] but with a new data set of higher quality. Here we use a modified version of a teleseismic inversion algorithm which includes some important new features in parameterization and regularization. In addition, the algorithm provides the possibility of realizing of different kinds of synthetic tests. Finally we compare the results of our tomographic inversion with the predictions derived from the thermomechanical model [11].

3. Data preparation

The data for this study come from the 48 stations of the DESERT network shown in Fig. 1. The DESERT network operated from April 2000 to May 2001. For the tomography investigation, 3366 travel times of P and PKP phases from 135 events at a distance range from 25° to 150° have been measured. The distributions of events are shown in Fig. 2A. It can be seen that the major part of the events used in this study is located in the Pacific area which corresponds to a back-azimuth segment from −10° to 90°. The arrival times were picked manually by one experienced person (Sergey Oreshin) for all stations of the network simultaneously thereby minimizing misidentification of the phases. The average number of records for one event is 25. The phases were picked only in a case if the seismogram around the arrival was coherent with seismograms recorded at other stations. Since the recording conditions were similar at all stations, the seismograms can be easily ranged with respect to each other to provide maximum correlation. As a result, the accuracy of the determination of relative arrival times appears to be rather high and is estimated as 0.1–0.15 s. All the data were uniformly weighted during inversion.

Reference travel times for all observed mantle and core phases are computed using the 1D reference model AK135 [27] and corrected for the station elevation and crustal thickness. The time correction for the station elevation is computed as follows:

$$\mathrm{d}t^{\mathrm{topo}} = \mathrm{d}h\sqrt{\sigma^2 - p^2},$$

where σ is the slowness in the uppermost layer and dh is the altitude of the station above sea level.

A time delay due to the Moho depth variation is included as an additional correction:

$$\mathrm{d}t^{\mathrm{moho}} = \mathrm{d}h\left[\sqrt{\sigma_1^2 - p^2} - \sqrt{\sigma_2^2 - p^2}\right],$$

where σ_1 and σ_2 are the values of slowness under and above the Moho interface, p is the ray parameter (horizontal component of the slowness vector), and dh is the relative Moho depth at the entry point with respect to the average crustal thickness in the reference model. For this

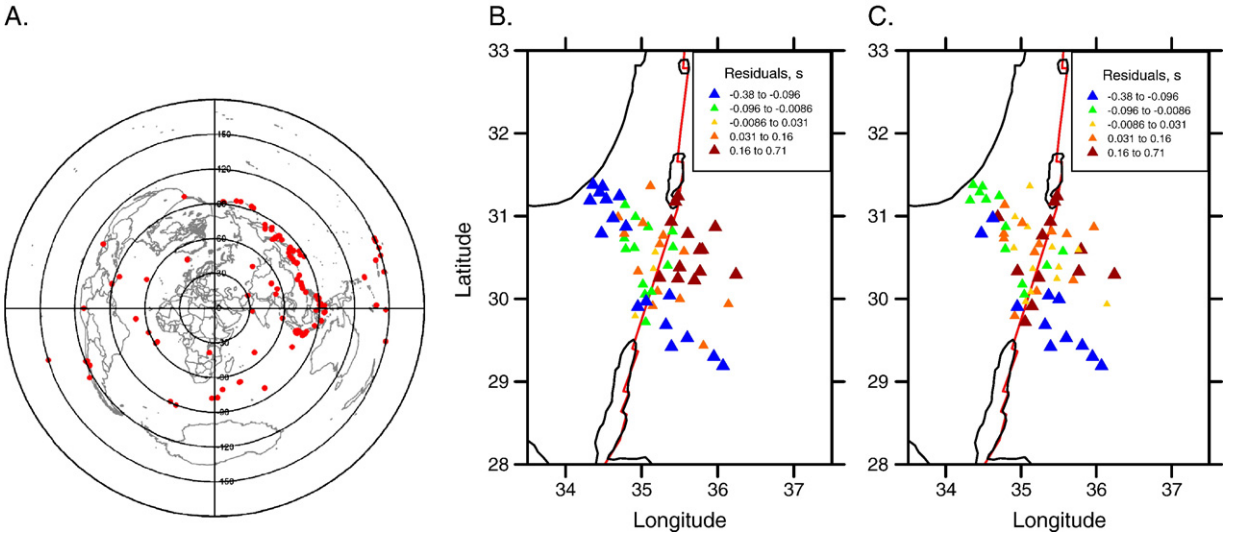

Fig. 2. A: Azimuthal-equidistant projection centered on the Dead Sea with distribution of 135 teleseismic events recorded by the DESERT network (rings of 30 to 180° distance). B, C: Average residuals at the stations before reduction for the relief and Moho depth (B.) and final residuals used for inversion (C.).

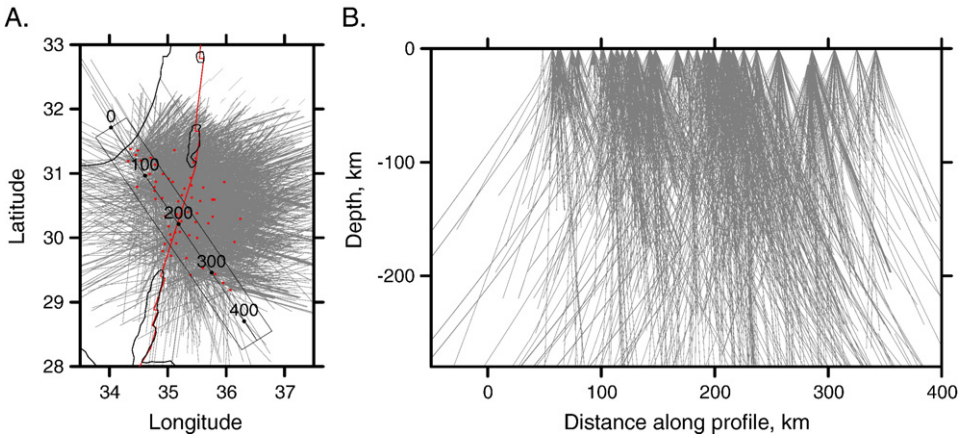

Fig. 3. Paths of the rays used in this study. A. Map projection of rays traced down to 280 km depth. Red points indicate station positions. B. Distribution of rays in a vertical profile. Position and width of the profile are shown in A.

study, we use the Moho depth map which was obtained as a result of tomographic inversion of regional Pn and Sn travel times in the Middle East and Eastern Mediterranean [20]. The final residuals are determined with respect to the average value, so that the sum of positive and negative residuals is zero. The average time residuals at all stations before correction for surface topography and Moho depth show systematically higher values east of the DST (Fig. 2B). However after the corrections this pattern becomes much less pronounced (Fig. 2C).

We do not consider the correction for the ellipticity of the Earth because the size of the study area is small (~200×250 km) and the variation of the ellipticity corrections at all stations for any source is negligible.

Ray paths projected to vertical and horizontal sections are shown in Fig. 3. It can be seen in the vertical section that the rays from different stations intersect below the depth of 10–30 km that is used to define the upper limit of the study volume (20 km depth).

4. Tomographic method

We use the general principle of teleseismic tomography which is defined in [1] and called as ACH algorithm.

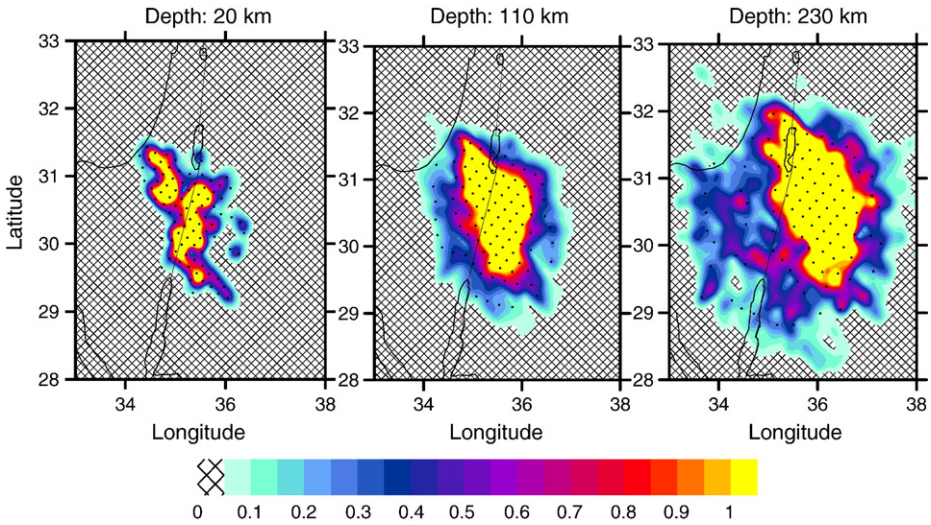

Fig. 4. Example of grid construction (black nodes) according to the ray density in three depth levels. Contour lines show normalized values of the ray density (1 of the scale corresponds to the following values of summary ray length in a cell 20×20×30 km: 2500 km at 20 km depth, 980 km at 110 km depth, 488 km at 230 km depth).

For each event, the residuals at all stations are computed relative to an average value. The resulting model is also relative with respect to a reference velocity model which cannot be retrieved from the teleseismic data. The inversion is performed with one linear iteration based on the rays traced in the 1D reference velocity model. The validity of this procedure is justified by the small magnitude of the resulting 3D anomalies.

An important feature of our inversion algorithm is the method of parameterization which is taken from regional studies [28,29]. The values of velocity anomalies are determined at nodes of a grid which are distributed in the study volume according to the ray density. Examples of the parameterization grids in some depth levels are shown in Fig. 4 together with the ray density plots. The velocity distribution between the nodes is defined using bilinear interpolation. The nodes are distributed at 15 horizontal levels from 20 km to 470 km depth, with steps of 30 km. At each level the nodes are located along parallel lines. The distance between nodes at each line depends inversely on the ray density. At the same time, we fix a minimum spacing between nodes in order to avoid an excessive concentration of nodes. The number of nodes at each level depends on the value of a fixed minimum spacing and varies from about 80 at the shallowest level to 150 at deep levels. It is important to note that the minimum grid spacing in the inversion is significantly smaller than the characteristic size of the reconstructed anomalies. In this case, the smoothness of the model is solely controlled by the regularization in the inversion step and not by the node distribution. To check this, we have performed the inversion using two grids with different values of minimum spacing, 10 and 20 km, and they provided very similar results.

It must be noted that the orientation of the lines in the grid can have some influence on the result. To

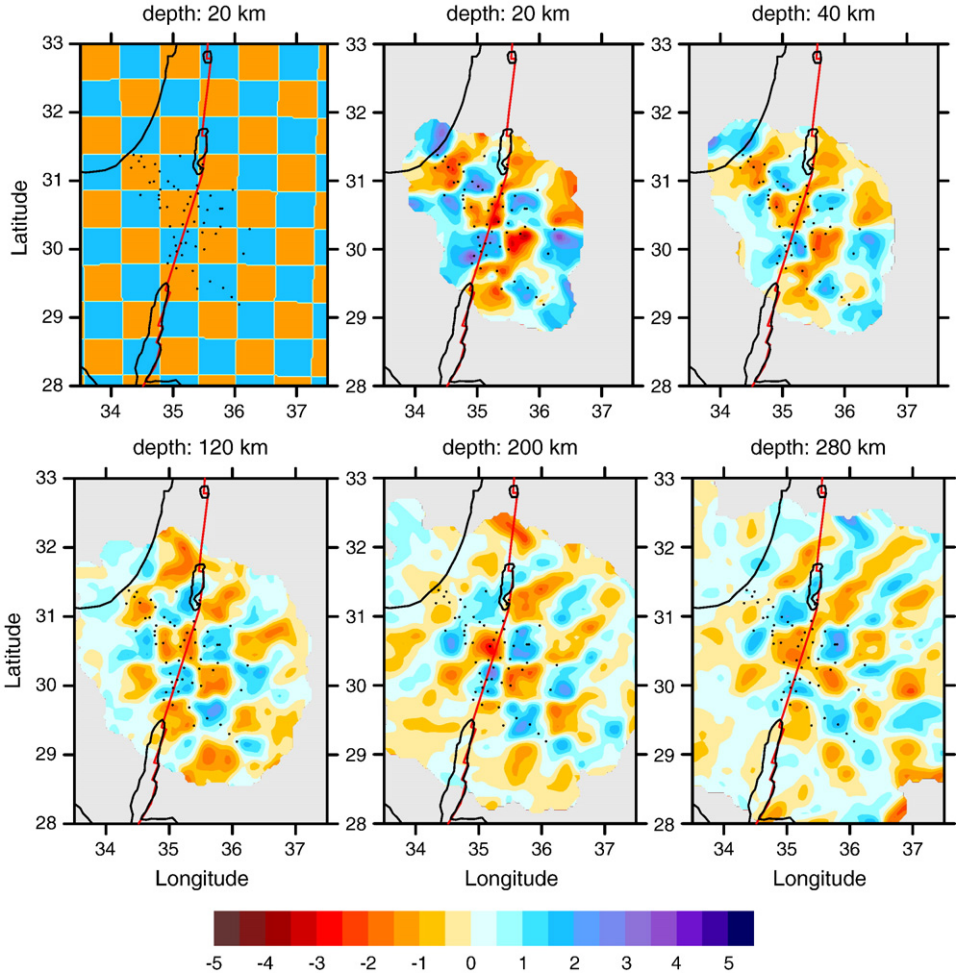

Fig. 5. Checkerboard test for the investigation of horizontal resolution. The initial model is a series of alternating columns with 60 km spacing in the horizontal direction and unlimited in the vertical direction. Amplitude of the initial anomalies is ±3%. Random noise with 0.15 s rms is added.

minimize this influence, the inversion is performed separately using four grids with different orientations (0°, 45°, 90° and 135°), and the results are stacked in one final map.

The inverse problem is based on solution of the following system of linear equations [1,3]:

$$\begin{array}{c}
(\partial t_1/\partial v_1)\mathrm{d}v_1 + (\partial t_1/\partial v_2)\mathrm{d}v_2 + \cdots + (\partial t_1/\partial v_n)\mathrm{d}v_n = \mathrm{d}t_1 \\
(\partial t_2/\partial v_1)\mathrm{d}v_1 + (\partial t_2/\partial v_2)\mathrm{d}v_2 + \cdots + (\partial t_2/\partial v_n)\mathrm{d}v_n = \mathrm{d}t_2 \\
\vdots \\
(\partial t_m/\partial v_1)\mathrm{d}v_1 + (\partial t_m/\partial v_2)\mathrm{d}v_2 + \cdots + (\partial t_m/\partial v_n)\mathrm{d}v_n = dt_m \\
\vdots \\
0 + 0 + 0 + \cdots + W^{\mathrm{smth}}\mathrm{d}v_{i1} + 0 + \cdots - W^{\mathrm{smth}}\mathrm{d}v_{i2} + 0 + \cdots + 0 = 0 \\
\vdots
\end{array}$$

where dv are the unknown velocity model parameters; dt are the observed residual times; W^{smth} is the predefined parameter for tuning the smoothing of the velocity model. The first derivative elements, $\partial t_i/\partial v_j$, i.e. the travel-time difference along the i-th ray due to a unit variation of the slowness at the j-th velocity parameter node, are computed by numerical integration along the rays constructed in the 1D spherical reference model. The smoothness of the resulting velocity anomalies is controlled by additional equations. Each of these contains only two terms with opposite signs and zero on the right side. To compose this block, we determine all possible pairs of neighboring nodes in the parameter grid. Here we present an example for the i-th pair (nodes $i1$ and $i2$). Increasing W^{smth} lowers the amplitude and smoothes the resulting anomalies. For the 1989 velocity parameters used in the inversion, the total number of rows in the matrix was 17,591, of which 3366 rows corresponded to the observed rays and 14,225 rows composed the additional smoothing block. Increasing the number of nodes in the parameter grid causes augmentation of the additional smoothing block.

The upper limit of the resolved area in teleseismic observation system is determined by the average spacing between the stations. For the teleseismic rays with epicentral distance range of 15°–95°, the dipping angles of the rays in the crust vary from 15° to 39°. Having the station spacing of 15–20 km, the sufficient ray intersection density is achieved at ~20 km depth. This is demonstrated in Fig. 3B with vertical projections of the ray paths. To take into account crustal effects above the resolved limit, some algorithms for teleseismic inversion include station corrections. In our case of a dense distribution of stations and their uniform calibration, the role of station correction parameters is played by the velocity perturbations at the first (20 km) depth level. In synthetic tests presented in the next section we investigate the effect of the crustal anomalies upon the deeper structures. We show that, although the vertical resolution of teleseismic tomography is rather poor, our observation system allows quite reliable distinguishing the upper crustal and lower crust/upper mantle effects.

The lower limit of the resolved area can also be estimated from the distribution of stations. Having the maximum size of the network at about 250 km and average dipping angles of teleseismic rays in the crust and upper mantle at 30–40°, the dippiest level in which we can have intersections of rays is about 150 km. At the same time, the inclusion of a significant amount of the PKP phases with much steeper rays allows us to shift the lower limit of the resolved area down to 260 km depth. The limits of the resolving areas can be also obtained from synthetic modes presented below. The checkerboard test (Fig. 5) shows that at 280 km depth the resolving capacity still remains satisfactory.

The effect of anomalies outside the study volume (i.e. from the bottom of the study volume to the source) is included in the velocity distribution at the lowermost levels. Although the parameter nodes are installed down to 470 km depth, only in the depth range from 20 km to 280 km is the density of the intersecting rays sufficiently high to provide reliable inversion results. Between 280 and 470 km, where the resolution becomes poor, the obtained anomalies are mostly related to outside factors and, in some sense, play the role of the source corrections.

The matrix is inverted using the LSQR method [30,31]. Interestingly, the data inversion provides only 36% variance reduction, which is unusually low for such a high quality data set.

5. Resolution tests

To investigate the resolution provided by the observation system, we have performed a series of synthetic tests with various input models and noise. Random noise is produced by a random number generator which provides a statistical distribution with the same histogram shape as that of the residuals in the ISC catalogue [10].

5.1. Checkerboard test

Here we present the results of reconstruction of a checkerboard model (Fig. 5). The input model consists of alternated 60 × 60 km columns with positive and negative velocity anomalies of ±3%. The noise with 0.15 s of RMS was added. The input model is reconstructed quite well in all depth levels below the region where the stations are located, and in slightly larger region at a depth of 120–200 km. However, resolution significantly decreases outside of that region.

5.2. Vertical resolution tests

To check the vertical resolution, we performed a series of tests presented in Fig. 6. We investigated combinations of three different types of anomalies: "CR — crustal" (±5% of amplitude), "LA — lithosphere" (±4%) and "M — mantle" (±3%) anomalies. Each type is represented by two anomalies of opposite signs. As in the checkerboard test, random noise with RMS of 0.15 s was added.

The tests with single-type anomalies (Models A–C in Fig. 6) show that , as expected, the teleseismic inversion does not provide good vertical resolution. All the retrieved anomalies are strongly smeared vertically. Neither amplitude, nor vertical location can be obtained reliably from these results. At the same time, these images can be easily distinguished from each other giving the general position of anomalies (crust, lithosphere, or mantle). It is a somewhat surprising result that the best vertical resolution is obtained in the case of the CR model.

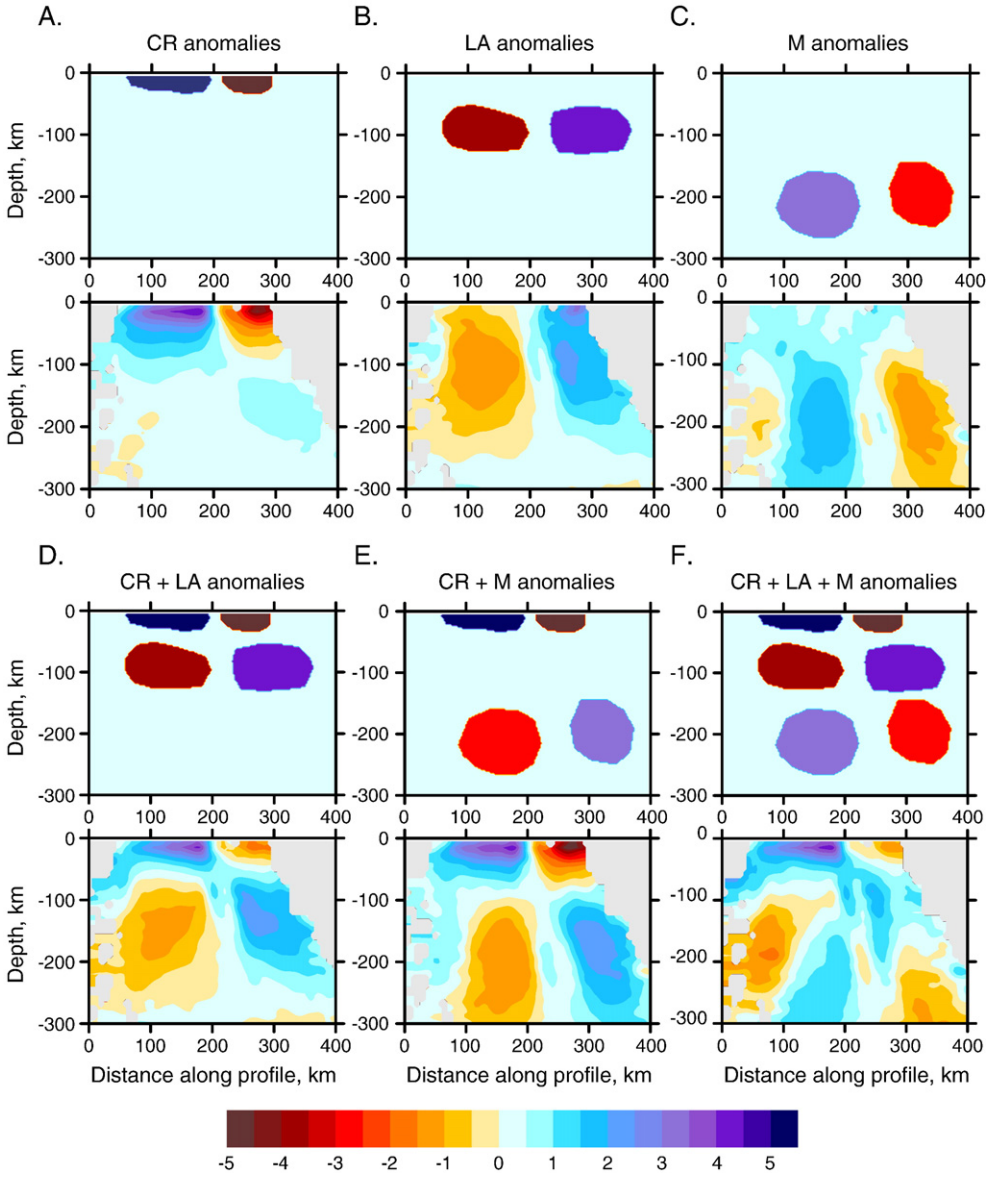

Fig. 6. Six tests for the investigation of the vertical resolution. The models are shown in a vertical section at 30.5° latitude. In each model, the upper image represents the initial distribution of anomalies and the lower image is a result of inversion. In all cases the random noise with 0.15 s of rms is added. Here we present different combinations of "CR" (crustal, ±5% of amplitude), "LA" (lithosphere–asthenosphere, ±4%) and "M" (mantle, ±3%) anomalies.

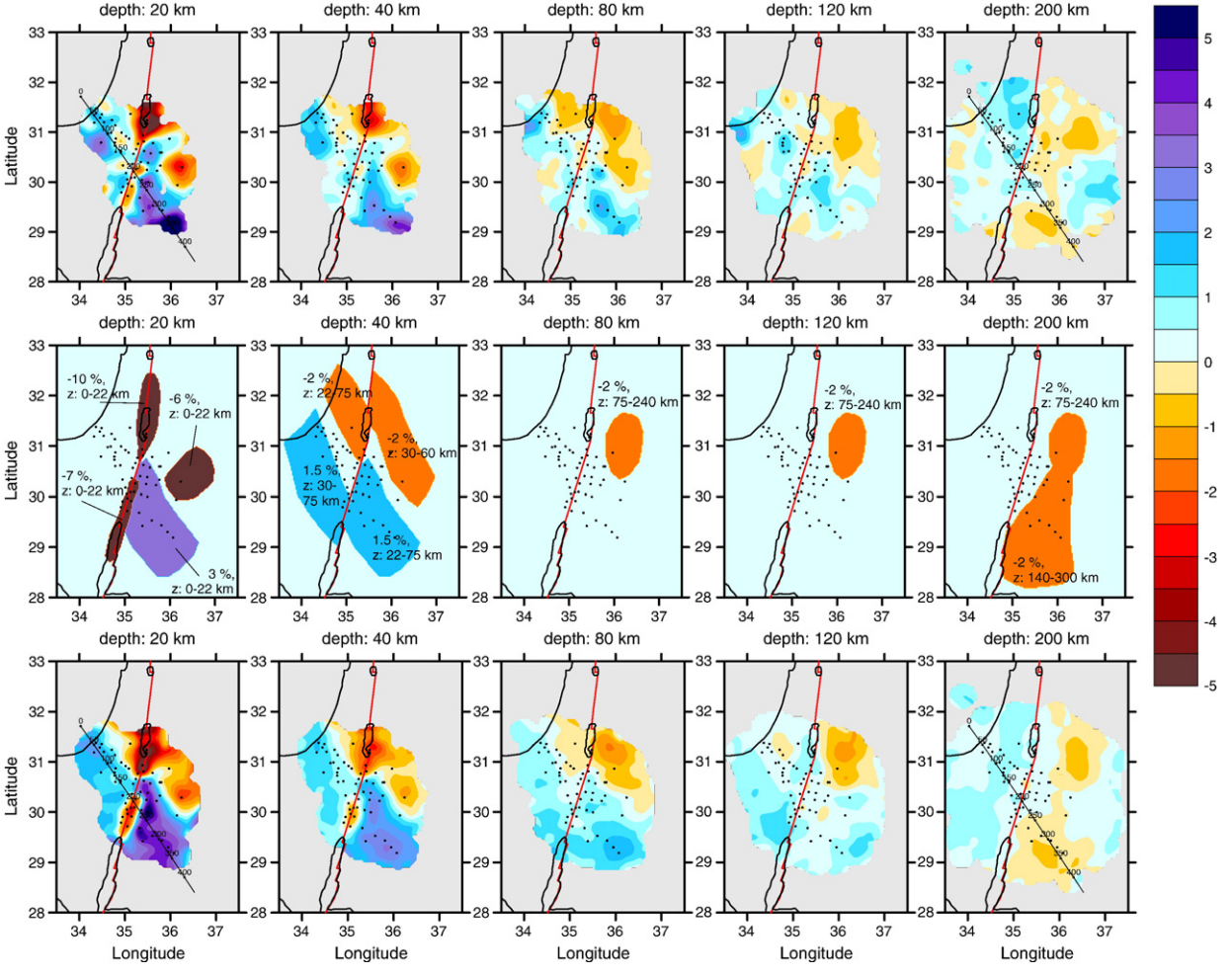

Fig. 7. Results of data and synthetic inversions in horizontal sections. The upper row represents P-velocity anomalies obtained after data inversion. The middle row shows the synthetic model with description of anomaly parameters (amplitude and depth interval). The lower row is the result of reconstruction of the synthetic model using the same ray configuration and parameters as in the data inversion case. Noise with an RMS of 0.14 s was added. It provided 35% variance reduction and 0.22 s of data RMS, similar to those observed in the case of the real data inversion.

In the case where all types of the anomalies are present simultaneously (CR+LA+M) our observation system does not allow retrieving such a complicated structure (Fig. 6, F). The reconstruction for the models CR+LA and CR+M (Fig. 6, D–E) also show the limitations of our results. The retrieved anomalies in these two cases have very similar shape. Thus we conclude that in this setting LA and M anomalies are hardly distinguished. At the same time, these images give evidence for relatively higher vertical resolution in the uppermost 100 km. In particular, the boundary between CR and LA anomalies (Model D), which is defined in the model at about 40 km depth, in the resulting images shifts to a depth of 50–60 km. If the boundary between the anomalies is at 150 km depth (between LA and M anomalies, Model F), the quality of recovering is poorer.

6. Results of inversion

The results of the inversion for P-velocity anomalies are presented in the upper row of Fig. 7 (horizontal sections) and in Fig. 8A (vertical section). The values are only shown if the distance to the nearest parameterization node is less than 20 km. Since the nodes are installed according to the ray density, the results are shown only in the areas where coverage allows sufficient horizontal resolution, also demonstrated by the checkerboard test (Fig. 5). As discussed, the model grid extends to a depth of 470 km, but we show and discuss here only the velocity anomalies in the depth interval of 20 to 280 km.

Maximum perturbations of about ±5% are observed in the uppermost layer (20 km depth). The result at this depth can be considered as an integral effect of the velocity perturbations in the upper crust where we observe strong negative anomalies beneath the Dead Sea basin and along the DST between the Gulf of Aqaba and the Dead Sea basin. Teleseismic studies cannot provide sufficient vertical resolution in the crust and therefore do not give an answer as to whether these anomalies are distributed throughout the crust or are concentrated in the uppermost several kilometers. At the same time, recent results of local-source tomography in the area [20] reveal similar features confirming the result for the top layer shown in Fig. 7. In particular, the local tomography model [20] shows the strongest negative anomaly in the uppermost section beneath the Arava Valley that can be associated with a thick layer of sediments (up to 10 km or more in the Dead Sea). At the same time, a significant low-velocity anomaly both in P and S velocities is observed beneath the DST throughout the crust. The likely reason for this is fracturing and/or alteration of rocks,

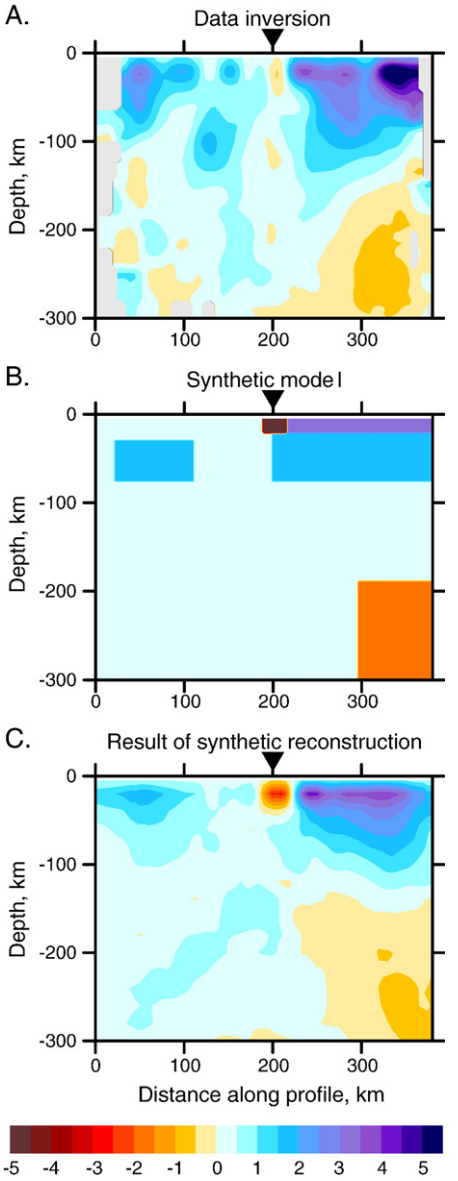

Fig. 8. Results of the data and synthetic inversions (same as in Fig. 7) presented in a vertical section. The position of the profile is indicated in Fig. 7 (20 and 200 km depth sections). A black inverted triangle marks the position of the DST. A. Result of data inversion. B. Initial synthetic model. C. Result of the synthetic model reconstruction.

which is also consistent with the high seismic anisotropy in the crust [22].

In our teleseismic results, the amplitudes of anomalies below the crust are fairly low. At 80 km depth under the Dead Sea basin, we observe anomalies with the amplitude of ±2%. Deeper, the amplitude of anomalies does not exceed ±1%. In the depth interval of 80 to 140 km we observe a high velocity anomaly crossing the DST from SE to NW and a parallel low-velocity anomaly

north of the high velocity anomaly. In the deeper sections (200 to 260 km) we observe a slight lowering of the P-velocity beneath the eastern flank of the DST. However, due to the low amplitude of these anomalies, it is not clear how reliable they are. In fact, for weak anomalies the signal to noise ratio becomes smaller and thus the reliability of inversion in this case is lower.

7. Synthetic model

The main purpose of this exercise is to find the configuration of synthetic anomalies to reproduce the velocity structure observed on the data inversion (Fig. 7, upper row) which would simultaneously have the same residuals RMS and variance reduction as the data. After a series of trials, we came out with a kind of minimum-structure model which is shown in the middle row of Fig. 7 and in Fig. 8B. The anomalies are represented by horizontal prisms with fixed thickness and fixed value of the velocity perturbations which are indicated in the maps.

It should be noted that this solution is just one of the possible solutions. In particular, there is a trade-off between the thickness of the anomaly and its amplitude. For example, all the anomalies in the depth interval between 0 and 22 km give the same effect as 10 km thick anomalies having twice the amplitude. In addition, as shown in Fig. 6, the depth resolution of this model is rather poor. Thus the depth intervals given in the maps of the initial anomalies should only be considered as very rough estimations. Moreover, in the case of opposite sign anomalies located one below another, their effect will be mutually canceled, and we would see much weaker amplitudes of the resulting anomalies. Therefore, we realize that other models could be proposed which provide the similar reconstruction of real images. At the same time, we believe that our synthetic model shown in Figs. 7 and 8 is among the simplest models that fit the data and which also have geodynamical meaning. We discuss these results in the next section.

The inversion has been performed with 0.14 s noise level. This noise level provides both the residual travel times RMS = 0.22 s and 35% variance reduction, similar to those observed in the data. The results of reconstruction are shown in the lower row of Figs. 7 and 8C. It can be seen that the reconstructed anomalies are quite similar in shape and amplitude with the results of the real data inversion (Fig. 7, upper row and Fig. 8A). Note that the retrieved anomalies have systematically lower amplitudes than the initial model, which is a common problem of the tomographic approach. At the same time, the results of this test can be used to estimate the true amplitude of anomalies in the Earth. If the inversion conditions in synthetic and real data inversions are similar (smoothing and variance reduction), and the retrieved synthetic model is similar to the data inversion results, it means that the synthetic model may be close to the real velocity distribution in the Earth.

8. Discussion

As was already mentioned above, the large negative anomalies in the upper crust are likely related to sedimentary basins and zones of high damage associated with the DST. A high-velocity anomaly in the upper crust east of the DST is likely associated with the uplift of the Precambrian basin imaged by other seismic studies with higher resolution in the crust [9]. Less clear is the nature of the strip-like anomalies located in the lower crust and/or mantle lithosphere. As it is shown in Fig. 7, those strip-like anomalies are probably crossing the DST, but may be significantly shifted along the DST by several tens of kilometers. It is important to indicate that the reliability of those anomalies is not equal. The high velocity anomaly in the south is crossing the region of the highest resolution (see Fig. 5). Its presence is even visible in the time residuals; see fast average time residuals at the southern stations in Fig. 2C. The low-velocity strip-like anomaly north of the high-velocity anomaly is located in the region of much lower resolution (see Fig. 5), and hence is less reliable compared to the high-velocity anomaly. We attribute the observed high velocities to the lithospheric heterogeneity in the region which existed before the DST was activated. Note that regionally the high velocity anomaly coincides with the domain of the high lower crustal velocities detected by the analyses of P-to-S seismic converted waves [23] and wide-angle reflections [9,21]. It is interesting that the data seem to not require a significantly anomalous mantle lithosphere below the DST itself. Some weak low-velocity anomalies in the mantle lithosphere which seem to continue DST to the depth in Fig. 8 may well result from down-smearing of the upper crustal anomalies. The conclusion about a seismically homogeneous mantle below the DST apparently contradicts the results of the SKS study by Rümpker et al [22], who suggest substantial variations of seismic anisotropy beneath the DST. However, this apparent contradiction is resolved if we consider that the travel time residuals of sub-vertical teleseismic P-waves sampling a vertical zone of strike–slip deformation, expected below the DST from the anisotropy study [22] and the thermo-mechanical model [11], are

close to zero, even if the shear strain and corresponding seismic anisotropy are high [32].

The geodynamic implication of the results obtained in this study is that presently there are no significant variations of temperature in the sub-Moho mantle and as a consequence not much topography of the lithosphere–asthenosphere boundary beneath the DST. This fact is also confirmed by a recent receiver function study by Mohsen et al. [24].

Now we can compare the estimated maximum amplitudes of the mantle anomalies with the predictions from the thermo-mechanical model [11]. The model predicts slightly lower mantle temperatures east of the DST than west of the DST at depths of 50–100 km, which is consistent with the tomographic image (Fig. 7). Predicted variations of average temperature in the 50–100 km depth range are less than 100 °C, which translates to less than 1% contrast in P-velocity [6]. Such small variations of seismic velocities are consistent with our tomographic model.

An intriguing feature of our model is a spotty low-velocity anomaly channeling the sub-lithospheric mantle down to 200–260 km and linking to the even deeper low-velocity anomaly at the south (Fig. 7). The geodynamic significance of this anomaly may be large, as it may reflect the complicated flow pattern of the relatively hotter material flowing from the deeper mantle from the south, i.e. from the region of the Red Sea Rift. However, we note that the low amplitude of this anomaly and relatively low horizontal resolution of our tomographic model in this region (see Fig. 5) indicates that this anomaly may be not real. Additional teleseismic tomography studies employing seismic stations arrays east of the Dead Sea and possibly also east of the Gulf of Aqaba would be required to clarify nature of this interesting anomaly.

Finally, it is interesting to compare our results with the results of teleseismic tomography across another classic continental transform fault, the Altyn Tagh fault (ATF), at the north edge of the Tibetan Plateau [5]. Similar to our results, a significant low-velocity anomaly is observed in the crust right beneath the ATF. However, contrary to the DST model, there is also a clear low-velocity anomaly in the upper mantle beneath the ATF down to a depth of 140 km [5]. We speculate that this remarkable difference may correspond to the major difference in the geodynamics of the DST and ATF. While the DST is almost a pure strike–slip fault [33,11], the ATF has a pronounced compression component [5], which may result in deep underthrusting of the continental crust beneath the ATF, generating low-velocity anomalies in the mantle (see Fig. 2A in [5]). We note that the expected seismic velocities, even in a fully eclogitized continental mafic crust are significantly lower than in mantle peridotites [34]. Alternatively, the different upper mantle velocity patterns beneath the DST and ATF may be due to the effect of shear heating in the upper mantle (also discussed in [5]), which can be expected to be more pronounced beneath the much faster slipping ATF. However, in this case the observed 5% reduction of the P-wave velocity in the uppermost mantle beneath the ATF would require at least a 500 °C temperature increase [6]. This may be compared with the 100 °C temperature increase modelled for the DST [11]. Whether a temperature increase of more than 500 °C in the uppermost mantle is really possible for the ATF setting, which at a first glance looks unlikely, should be analysed by thermo-mechanical modelling.

Acknowledgments

This study was supported by the DESERT project of the DFG and GFZ, and by ESRA, MNI, Israel. The data for the DESERT array were collected with instruments from the Geophysical Instrument Pool Potsdam. We thank Jim Mechie for unselfish help in editing the manuscript as well as anonymous reviewers and Editor (Rob Van der Hilst) for their helpful comments.

References

[1] K. Aki, A. Christofferson, E.S. Husebye, Determination of the three dimensional structure of the lithosphere, J. Geophys. Res. 82 (1977) 277–296.

[2] U. Achauer, A study of Kenya rift using delay time tomography analysis and gravity modelling, Tectonophysics 209 (1992) 197–207.

[3] J. Evans, U. Achauer, Teleseismic velocity tomography using the ACH method: theory and application to continental scale studies, in: H. Iyer, K. Hirahara (Eds.), Seismic Tomography: Theory and Practice, Chapman and Hall, London, 1994, pp. 319–360.

[4] I.Yu Kulakov, S.A. Tychkov, S.I. Keselman, Three-dimensional structure of lateral heterogeneities in P-velocities in the upper mantle of the southern margin of Siberia and its preliminary geodynamical interpretation, Tectonophysics 241 (1995) 239–257.

[5] G. Wittlinger, P. Tapponier, G.J. Poupinet, J. Mei, S. Danian, G. Herquel, F. Masson, Tomographic evidence for localized lithospheric shear along the Altyn Tagh Fault, Science 282 (1998) 74–76.

[6] S.V. Sobolev, H. Zeyen, G. Stoll, F. Werling, R. Altherr, K. Fuchs, Upper mantle temperatures from teleseismic tomography of French Massif Central including effects of composition, mineral reactions, anharmonicity, anelasticity and partial melt, Earth Planet. Sci. Lett. 139 (1996) 147–163.

[7] S.V. Sobolev, H. Zeyen, M. Granet, U. Achauer, C. Bauer, F. Werling, R. Altherr, K. Fuchs, Upper mantle temperature and lithosphere–asthenosphere system beneath the French Massif Central constrained by seismic, gravity, petrologic and thermal observations, Tectonophysics 275 (1997) 143–164.

[8] DESERT Group, Multinational geoscientific research effort kicks off in the Middle East, Eos 81 (609) (2000) 616–617.
[9] DESERT Group, The crustal structure of the Dead Sea Transform, Geophys. J. Int. 156 (2004), doi:10.1111/j.1365-246X.2004.02143.x.
[10] International Seismological Centre, Bulletin Disks 1–9 [CD-ROM], Internatl. Seis. Cent., Thatcham, United Kingdom, , 2001.
[11] S.V. Sobolev, A. Petrunin, Z. Garfunkel, A. Babeyko, DESERT Group, Thermo-machanical model of the Dead Sea Transform, Earth Planet. Sci. Lett. 238 (2005) 78–95.
[12] J. Makris, Z. Ben-Avraham, A. Behle, A. Ginzburg, P. Giese, L. Steinmetz, R.B. Whitmarsch, S. Eleftheriou, Seismic refraction profiles between Cyprus and Israel and their interpretation, Geophys. J. R. Astron. Soc. 75 (1983) 575–591.
[13] Z. El-Isa, J. Mechie, C. Prodehl, J. Makris, R. Rihm, A crustal structure study of Jordan derived from seismic refraction data, Tectonophysics 138 (1987) 235–253.
[14] A. Ginzburg, Z. Ben-Avraham, A seismic refraction study of the north basin of the Dead Sea, Israel, Geophys. Res. Lett. 24 (16) (1997) 2063–2066.
[15] D. Seber, M. Vallve, E. Sandvol, D. Steer, M. Barazangi, Middle East tectonics: applications of geographic information systems (GIS), GSA Today 7/2 (1997) 1–6.
[16] A. Al-Zoubi, Z. Ben-Avraham, Structure of the Earth's crust in Jordan from potential field data, Tectonophysics 346 (2002) 45–59.
[17] E. Sandvol, D. Seber, A. Calvert, M. Barazangi, Grid search modelling of receiver function: Implications for crustal structure in the Middle East and North Africa. J. Geophys. Res. 103 (b11) (1998) 26, 899–26, 917.
[18] A. Hofsteter, G. Bock, Shear-wave velocity structure of the Sinai subplate from receiver function analysis, Geophys. J. Int. 158 (2004) 67–84.
[19] A. Ginzburg, Z. Ben-Avraham, Crustal structure and tectonic processes in the Levant and the eastern Mediterranean, Isr. J. Earth-Sci. 40 (1992) 125–133.
[20] I. Koulakov, S.V. Sobolev, Moho depth and 3D P and S structure of the crust and uppermost mantle in the Eastern Mediterranean and Middle East derived from tomographic inversion of local ISC data, Geophys. J. Int. 164 (1) (2005) 218–235.
[21] J. Mechie, K. Abu-Ayyash, Z. Ben-Avraham, R. El-Kelani, A. Mohsen, G. Rümpker, J. Saul, M. Weber, Crustal shear velocity structure across the Dead Sea Transform from two-dimensional modelling of DESERT project explosion seismic data, Geophys. J. Int. 160 (2005) 910–924, doi:10.1111/j.1365-246X.2005.02526.x.
[22] G. Rümpker, T. Ryberg, G. Bock, Desert Seismology Group, Evidence for boundary-layer mantle flow beneath the Dead Sea Transform from seismic anisotropy, Nature 425 (2003) 497–501.
[23] A. Mohsen, R. Hofstetter, G. Bock, R. Kind, M. Weber, K. Wylegalla, G. Rümpker, DESERT Group, A receiver function study across the Dead Sea Transform, Geophys. J. Int. 160 (2005) 948–960.
[24] A. Mohsen, R. Kind, S.V. Sobolev, M. Weber, Thickness of Lithosphere at the Dead Sea Transform, Geophys. J. Int. (2006), doi: 10.1111/j.1365-246X.2006.03185.x.
[25] O. Ritter, T. Ryberg, U. Weckmann, A. Hoffmann-Rothe, A. Abueladas, Z. Garfunkel, DESERT Research Group, Geophysical images of the Dead Sea Transform in Jordan reveal an impermeable barrier for fluid flow, Geophys. Res. Lett. 30 (2003), doi:10.1029/2003GL017541.
[26] R. Hofstetter, C. Dorbath, M. Rybakov, V. Goldshmidt, Crustal and upper mantle structure across the Dead Sea rift and Israel from teleseismic P-wave tomography and gravity data, Tectonophysics 327 (2000) 37–59.
[27] B.L.N. Kennett, E.R. Engdahl, R. Buland, Constraints on seismic velocities in the Earth from traveltimes, Geophys. J. Int. 122 (1995) 108–124.
[28] I.Yu Koulakov, 3D tomographic structure of the upper mantle beneath the central part of Eurasian continent, Geophys. J. Int. 133 (2) (1998) 467–489.
[29] I.Yu Koulakov, S. Tychkov, N. Bushenkova, A. Vasilevskiy, Structure and dynamics of the upper mantle beneath the Alpine–Himalayan orogenic belt, from teleseismic tomography, Tectonophysics 358 (2002) 77–96.
[30] C.C. Paige, M.A. Saunders, LSQR: an algorithm for sparse linear equations and sparse least squares, ACM Trans. Math. Softw. 8 (1982) 43–47.
[31] A. Van der Sluis, H.A. van der Vorst, Numerical solution of large, sparse linear algebraic systems arising from tomographic problems, in: G. Nolet (Ed.), Seismic Tomography, Reidel, Dortrech, 1987, pp. 49–83.
[32] S.V. Sobolev, A. Grésillaud, M. Cara, How robust is isotropic delay time tomography for anisotropic mantle? Geophys. Res. Lett. 26 (1999) 509–512.
[33] Z. Garfunkel, Internal structure of the Dead Sea leaky transform (rift) in relation to plate kinematics, Tectonophysics 80 (1981) 81–108.
[34] S.V. Sobolev, A.Yu Babeyko, Modeling of mineralogical composition, density and elastic wave velocities in anhydrous magmatic rocks, Surv. Geophys. 15 (1994) 515–544.